GEOPHYSICS, VOL. 82, NO. 5 (SEPTEMBER-OCTOBER 2017); P. E243–E256, 15 FIGS., 2 TABLES.
10.1190/GEO2016-0109.1

Check for updates

Downloaded 08/31/18 to 93.174.129.117. Redistribution subject to SEG license or copyright; see Terms of Use at http://library.seg.org/

Correlation analysis for spread-spectrum induced-polarization signal processing in electromagnetically noisy environments

Weiqiang Liu[1], Rujun Chen[2], Hongzhu Cai[3], Weibin Luo[4], and André Revil[5]

ABSTRACT

In induced-polarization (IP) surveys, the raw data are usually distorted significantly by the presence of electromagnetic (EM) interferences, including cultural noise. Several methods have been proposed to improve the signal-to-noise ratio of these data. However, signal processing in an electromagnetically noisy environment is still a challenging problem. We have determined a new and simple technique based on the analysis of the correlation between the measured potential and the injected primary current signals. This processing is applied to the data acquired using a new frequency-domain IP method called the spread-spectrum induced-polarization (SSIP) approach. In this approach, we use a pseudorandom m-sequence (also called the maximum length sequence) for the injected primary current. One of the advantages of this sequence is to be essentially spectrally flat in a given frequency range. Therefore, complex resistivity can be determined simultaneously at various frequencies. A new SSIP data set is acquired in the vicinity of Baiyin mine, Gansu Province, China. The correlation between potential difference and transmitting current signals for each period can be used to assess data quality. Only when the correlation coefficient between the two signals is greater than 0.5 can the SSIP data be used for subsequent processing and tomography. We determine what threshold value should be used for the correlation coefficient to extract high-quality apparent complex resistivity data and eliminate EM-contaminated data. We then compare the pseudosections with and without using the correlation analysis. When the correlation analysis is used, the noisy data are filtered out, and the target anomaly obtained through tomography is clearly enhanced. The inversion results of the apparent complex resistivity (amplitude and phase) for the survey area are consistent with some independent geologic and drilling information regarding the position of the ore body demonstrating the effectiveness of the approach.

INTRODUCTION

Nowadays, electrical and electromagnetic (EM) methods are broadly applied to environmental and geotechnical problems (see, for instance, Pellerin, 2002). Induced polarization (IP) is a powerful geophysical technique looking at the reversible charge storage in porous media. The first IP investigations were conducted in the time domain at the turn of the twentieth century (Schlumberger, 1920). At the end of the 1950s, Collett (1959) and Seigel (1959) propose a frequency-domain approach to IP (FDIP). In the following decades, various variants of the FDIP methods have been proposed. For instance, Wait (1959) proposes a variable-frequency method, Zonge and Wynn (1975) develop the concept of complex resistivity measurements (measuring the amplitude and the phase), whereas He (1993) and Han et al. (2013) develop the concept of the dual-frequency IP method. More recently, Chen et al. (2007) develop the pseudorandom multifrequency method, and Xi et al. (2013, 2014) introduce the spread spectrum IP (SSIP) method that is going to be

Manuscript received by the Editor 4 March 2016; revised manuscript received 8 March 2017; published ahead of production 27 May 2017; published online 05 July 2017.
[1]Central South University, School of Geosciences and Info-Physics, Changsha, China and Institute of Geophysical and Geochemical Exploration, Chinese Academy of Geological Sciences, Langfang, China. E-mail: liuweiqiang15@mails.ucas.ac.cn.
[2]Central South University, School of Geosciences and Info-Physics, and Key Laboratory of Metallogenic Prediction of Nonferrous Metals and Geological Environment Monitoring, Changsha, China. E-mail: chrujun12358@gmail.com.
[3]University of Utah, Consortium for Electromagnetic Modeling and Inversion (CEMI), Salt-Lake City, Utah, USA. E-mail: caihongzhu@hotmail.com.
[4]Gansu Non-ferrous Geological Survey Institute, Lanzhou, China. E-mail: lwbcsu@163.com.
[5]Université Savoie Mont Blanc, CNRS, IRD, IFSTTAR, ISTerre, Chambéry, France. E-mail: andre.revil@univ-smb.fr.
© 2017 Society of Exploration Geophysicists. All rights reserved.

Downloaded 08/31/18 to 93.174.129.117. Redistribution subject to SEG license or copyright; see Terms of Use at http://library.seg.org/

used in this paper. The main difference between these different FDIP methods is the type of signal used for the injected (primary) current. The SSIP method is, therefore, a quite recent FDIP method based on the use of an m-sequence for the primary current. The m-sequence is a pseudorandom binary sequence that is periodic and is able to mimic every binary sequence (except the zero vector). The m-sequence is spectrally flat with the exception of the DC component (Duncan et al., 1980). Because the m-sequence is intrinsically a broadband signal (Ziolkowski et al., 2007), the complex resistivity can be simultaneously determined at various frequencies. Then, the subsurface can be imaged through tomography of the complex resistivity data (amplitude and phase).

In geophysical exploration, the acquired or raw IP data may be significantly distorted by the presence of a high level of noise. Various methods have been proposed to improve the signal-to-noise ratio (S/N) in IP surveys (Pelton et al., 1978; Brown, 1985; Routh and Oldenburg, 2001; Li et al., 2013; Ilyichev and Bobrovsky, 2015; Larsen, 2016; Larsen and Behroozmand, 2016; Olsson et al., 2016). In SSIP, the survey is similar to the classical galvanometric electrical prospecting methods, such as DC resistivity and magnetoresistivity methods. The components of the electrical fields are measured with voltage electrodes (stainless steel electrodes or eventually nonpolarizable electrodes), which can easily be contaminated by EM interference caused by cultural and natural noise sources. There are many sources that produce strong EM interference, such as telluric currents, stray currents, power lines, the cathodic protection of underground pipes, and grounded equipment. These issues are obviously more serious when the survey area is located in the vicinity of mining operations (Szarka, 1988; Junge, 1996). The noise interference can cause significant errors for the calculation of complex resistivity, which could lead to wrong interpretations of the subsurface structure and the localization of the geologic targets and ore bodies.

The digital filter and mean stack methods are commonly used for noise suppression in various FDIP methods (see Chen et al., 2007, 2010). Digital filters, such as high-pass, low-pass, band-pass, and notch filters, are simple methods that are widely used to suppress or attenuate the effects of noise. However, there is a sometimes a large overlap between the noise spectra of different noise sources and SSIP signal spectra. This issue makes classical digital filters usually ineffective. The mean stack method can suppress and improve the S/N when the noise corresponds to a random Gaussian noise. It can also attenuate the effect of occasional spike impulse noise by extending the observation time. That said, it cannot suppress repeated spike impulse-type noise. Moreover, the stacking method cannot evaluate the data quality for each period or select the data with high S/N. Robust stacking is effective to reduce outliers caused by spike impulse noise and improve data processing quality. However, the percentage of outliers cannot exceed 50% for each sample (Buselli and Cameron, 1996; Streich et al., 2013; Liu et al., 2015, 2016).

In this paper, we are interested in applying correlation analysis to SSIP signal processing in very electromagnetically noisy environments. This technique has already been successfully applied to magnetotelluric and seismic signals processing (Bahorich and Farmer, 1995; Saraev et al., 2012). However, the method has never been applied to FDIP data processing. For multiperiod SSIP data obtained during the same survey, when the observed potential signal is of good quality, the correlation between the primary current data and the measured potential data is expected to be high. In contrast, when the measured potential signals are contaminated significantly by EM interferences and background Gaussian noise, the correlation between the injected current and the potential data is low because the additive noise is uncorrelated with the primary current data. We can therefore calculate the correlation coefficient between the primary current data and the measured potential difference data for each period and set a threshold for the correlation coefficient according to the simulated noise and actual SSIP signals to extract the data characterized by the highest quality and filter out low-quality data. By stacking the high-quality SSIP data kept after correlation analysis, we can get a more accurate complex resistivity data set compared with the complex resistivity data obtained using the classical mean stack method. In this paper, we demonstrate the efficiency and effectiveness of our processing approach by analyzing a new data set of SSIP data acquired in a very noisy survey area in the vicinity of Baiyin mine, Gansu Province, China.

SSIP METHOD: PRESENTATION AND CASE STUDY

The SSIP method is a new FDIP method using an m-sequence for the primary source current in IP surveys (Xi et al., 2013, 2014). The spread spectrum m-sequence is a binary sequence generated using maximal linear feedback shift registers. The length of L-order m-sequence is $2^L - 1$, where L is the number of shift registers. The spectrum of the m-sequence is quite flat (except for the DC component), similar to the spectrum of random signal. The use of the m-sequence is very popular in digital communication systems that use direct-sequence spread spectrum and frequency-hopping spread spectrum transmission systems (see Golomb, 1994).

This paper is based on a new SSIP data set acquired with strong injected primary currents (approximately 8–20 A) and long-time data acquisition (maximum 40 min for current injection with strong interferences) beside the Baiyin mine in Gansu province of northwest of China. The survey area is located east of the Beiqilian Caledonian fold (Liu et al., 2015). A decade ago, Baiyin was the biggest copper producer in China, but its copper resources are currently running out. This has prompted the need for new exploration surveys with the hope to keep industrial activity in this region at its highest level. Different geophysical instruments and methods have been applied in this area for the purpose of finding new ore bodies. These methods include time-domain IP (TDIP), controlled-source audio-magnetotelluric (CSAMT), and time-domain electromagnetic data (TEM). Because of the strong EM interference caused by many spurious sources, only a few instruments or methods can satisfy the data quality requirement needed for ore body localization. Recently, our group has carried out several surveys using the SSIP approach in a specific area characterized by a fault system hosting a lead and zinc deposit. The present paper is focused on a 2D SSIP survey line using the general gradient array protocol. This survey is centered on the top of the ore body. It consists of 101 potential electrodes located over 2 km (from −1000 to 1000 m) with a 20 m spacing between the electrodes along the survey.

During the acquisition, the spacing between current electrodes A and B ranges from 20 to 5200 m. There are 34 current injections inside and outside the receiver array to ensure the high resolution of near-surface structures. The initial current electrode spacing between A and B is set to be 20 m. Then, it is increased to 80 m each time linearly from 20 to 2020 m (e.g., $AB = 20$, 100,

Downloaded 08/31/18 to 93.174.129.117. Redistribution subject to SEG license or copyright; see Terms of Use at http://library.seg.org/

180, 260, 340, ..., 1860, 1940, 2020 m). Finally, this spacing is increased to 400 m each time linearly from 2400 to 5200 m (e.g., $AB = 2400$, 2800, 3200, 3600, 4000, 4400, 4800, and 5200 m). The number of acquired quadrupoles is 100×34, so a total of 3400 quadrupoles can be used in principle for this survey. However, the exact number of acquired quadrupoles is smaller than 3400 because of voltage signal saturation near the current electrodes and the low S/N at some remote locations and at some frequencies. The number of valid quadrupoles for the first frequency is 2631, approximately 77.4% of the theoretical value of 3400 measurements. The survey line (located along a north–south direction) is roughly perpendicular to the fault system hosting the ore body. Survey sites start from −1000 m in the south to 1000 m in the north. Figure 1 illustrates the gradient array protocol we used with various current electrode spacings used along the survey line.

The receiver array is based on GPS sync and the ZigBee network with a total of 25 receivers (100 channels, see details in Xi et al., 2014). As mentioned above, the transmitting (primary) current is five-order spread spectrum m-sequence at clock cycle of 0.5 s. The period of the transmitting current is 16 s, and the sampling frequency is 64 Hz. The amplitude of the transmitting current is 8 A when the interference is the strongest, and there are 1024 samples in each period. The time for data acquisition is roughly 40 min (approximately 160 periods) when the interference is the strongest. By using a five-order m-sequence for the excitation current, the complex resistivity can be obtained for a set of frequencies simultaneously. The apparent complex resistivity $\rho(f)$ in SSIP can be obtained in a way similar to the traditional FDIP approaches; i.e.,

$$\rho(f) = K\frac{U(f)}{I(f)}, \tag{1}$$

where $U(f)$ denotes the frequency spectrum of the potential difference data, $I(f)$ is the frequency spectrum of synchronous primary current data, and K corresponds to the geometric factor given by (Schlumberger, 1920)

$$\frac{1}{K} = \frac{1}{2\pi}\left[\left(\frac{1}{AM} - \frac{1}{BM}\right) - \left(\frac{1}{AN} - \frac{1}{BN}\right)\right]. \tag{2}$$

In equation 2, A and B denote the current electrodes, whereas M and N denote the voltage electrodes (AM, BM, AN, and BN denote the spacing between the corresponding electrodes, e.g., Schlumberger, 1920; Barker, 1981).

The frequency spectrum of the time series signal can be calculated through a discrete Fourier transform (DFT), which is efficiently implemented via the fast Fourier transform algorithm (Oppenheim, 1989). The sequence of real numbers is transformed into a sequence of complex numbers by the DFT according to the formula

$$X_k = \sum_{n=0}^{N-1} x_n e^{-\frac{2\pi i}{N}kn}, \quad \text{for } k = 0, \ldots, N-1. \tag{3}$$

The frequency spectrum of the m-sequence is relatively flat in the frequency range of 1/16–1 Hz. Therefore, to guarantee the signal strength, we only calculate the apparent complex resistivity data in the frequency range of 1/16–1 Hz (the second to seventeenth frequency points) using the injected primary current and the measured potential difference data. For simplicity, we calculate the mean of the complex resistivity only at four discrete frequencies. Finally, for each independent quadrupole, we can get the complex resistivity at 2.5/16 Hz (i.e., 0.16 Hz), 6.5/16 Hz (i.e., 0.41 Hz), 10.5/16 Hz (i.e., 0.66 Hz), and 14.5/16 Hz (i.e., 0.91 Hz). Once the filtering technique is accomplished, the resistivity and chargeability of the subsurface can be imaged by inverting the apparent complex resistivity data.

In contrast to the classical rectangular current waves with boxes of constant durations, the m-sequence is a broadband signal. The power of this signal, in the frequency range of 1/16–1 Hz, is quite uniformly flat. Figure 2 illustrates the difference between the classical rectangular and m-sequence transmitted current waves of two periods, respectively (period of 16 s and amplitude of 8 A). The duty cycle of the rectangular wave is 50%. Figure 3 shows the amplitude spectrum of these two signals in the frequency range of 0–1 Hz. For the rectangular wave sequence, the amplitude varies

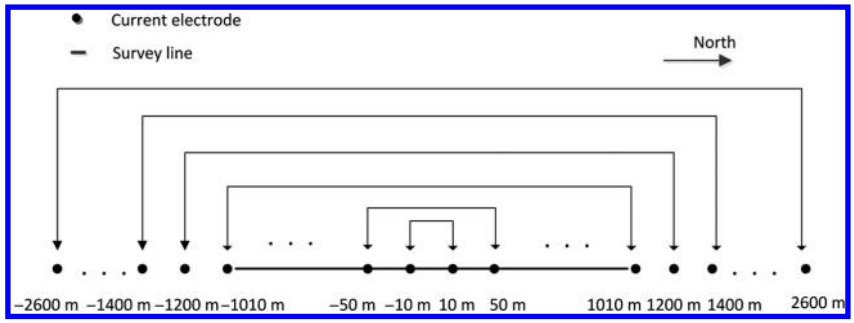

Figure 1. Nonconventional gradient array protocol for the survey line. Current was supplied using 34 current electrodes groups with a maximum current electrode spacing of 5200 m and a minimum spacing of 20 m. The length of the line is 2000 m with spacing between the potential electrodes of 20 m.

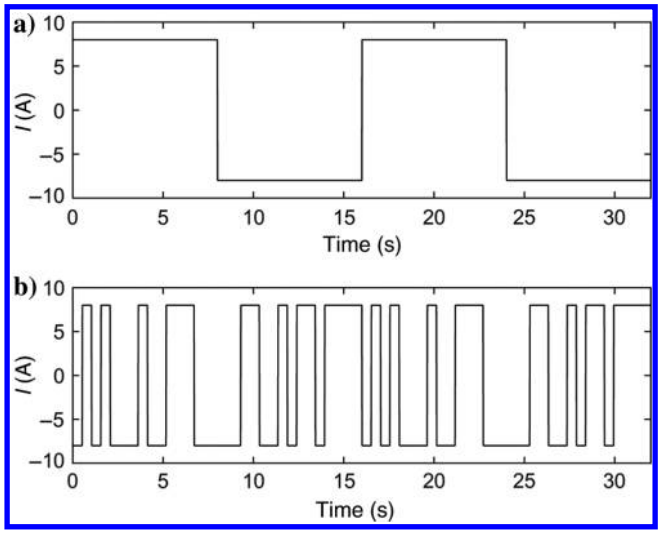

Figure 2. Waveform for the injected primary current I (in A). (a) Classical rectangular wave with two periods. (b) Spread spectrum five-order m-sequence wave of two periods.

Downloaded 08/31/18 to 93.174.129.117. Redistribution subject to SEG license or copyright; see Terms of Use at http://library.seg.org/

inversely with the frequency. The power of the signal is mainly concentrated at odd harmonics. The sum of the amplitude for the first three frequencies at 1/16, 3/16, and 5/16 Hz occupies 75.84% of all the eight frequencies. The amplitude at 1/16 Hz is 10.2 A; however, the amplitude at 15/16 Hz is only 0.7 A. In contrast, for five-order m-sequence, the sum of the amplitude for the first three frequencies at 1/16, 2/16, and 3/16 Hz occupies 21.53% of all 16 frequencies. The amplitude at 1/16 Hz is 2.9 A, and the amplitude at 1 Hz is 1.8 A. Therefore, apparent complex resistivity data with similar S/N at 16 frequencies can be calculated simultaneously by transmitting the five-order m-sequence current and measuring the resulting potential differences at the recording voltage electrodes.

From what was explained above, it is now clear that the main advantage of the SSIP technique is the improvement of the efficiency in getting a multifrequency survey done at once. In other words, the time required to carry out the survey can decrease substantially compared with use of harmonic primary current at a set of distinct frequencies (except possibly if several harmonic currents at different frequencies are simultaneously injected and the deconvolution of the signals is performed after the survey). In addition, in traditional FDIP surveys, the excitation of the subsurface at a set of distinct frequencies injected at different times implies that the noise for each frequency may be different, so different processing methods may be required to process the raw data. For SSIP, the apparent complex resistivity is measured at various frequencies, and at the same time, so they can be processed simultaneously using the same technique. However, a broad frequency band also produces a lower S/N at each investigated frequency for SSIP, so high-power injected current and effective signal processing methods are still necessary in a very noisy environment.

CORRELATION ANALYSIS METHOD

Correlation analysis algorithm

Correlation analysis is a mathematical technique used to measure the similarity and to study changes in measured (possibly 2D or multidimensional) signals. This method has been successfully applied to process magnetotelluric and seismic data. In the magnetotelluric method, the correlation between the natural electric and magnetic fields can be used to evaluate the S/N of magnetotelluric signals. When the S/N is high, correlation is also high. In contrast, when the S/N is low, the correlation is also low (see Reddy and Rankin, 1974; Lamarque, 1999). This method has also been used in the realm of seismic exploration. The correlation coefficient between seismic traces can be used to represent the trace-to-trace similarity. Similar traces are mapped with high correlation coefficients and discontinuities have low coefficients (Bahorich and Farmer, 1995).

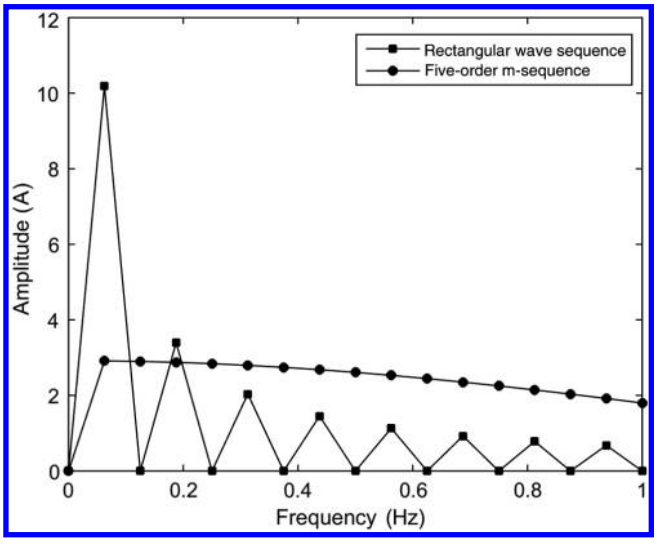

Figure 3. Amplitude spectrum between 0 and 1 Hz of the five-order m-sequence and the classical rectangular wave sequence (used usually in time-domain IP) with the same current amplitude of 8 A.

There are several types of correlation analysis algorithms to characterize the strength of the statistical relationship between two random variables, including the Spearman rank-order correlation (Ramsey, 1989), the biserial correlation approach (Tate, 1954), the Phi correlation method (Kuhn, 1973), and the product moment correlation coefficient (PMCC) method (Gayen, 1951), just to cite few of them (for a discussion on this family of methods, see Stigler, 1989). PMCC is a convenient algorithm that has been broadly used in geophysics. We consider the random vectors x_i and y_i, $i = 1, 2, 3, \ldots, n$. The PMCC correlation coefficient is computed as

$$C = \frac{\sum_{i=1}^{n}(x_i - \bar{x})(x_i - \bar{y})}{\sqrt{\sum_{i=1}^{n}(x_i - \bar{x})^2 \sum_{i=1}^{n}(y_i - \bar{y})^2}}, \tag{4}$$

where $\bar{x}$ and $\bar{y}$ denote the mean value of the components of the vectors x and y, respectively. The PMCC coefficient lies in the range of -1 to 1. A value of zero indicates that there is no correlation between the two variables. A value greater than 0 indicates a positive correlation; that is, the value of one variable increases with the increase of the other variable and vice versa. A PMCC value of less than 0 indicates some anticorrelation between the two variables. There are advantages in taking the PMCC approach to calculate the correlation coefficient of two variables. These two variables can be measured in entirely different units. The PMCC of the two variables will stay unchanged if one variable is multiplied by a constant or a constant number is added to the variable. These properties allow the correlation to be comparable and not affected by the units and scale of the variables such as transmitted current and potential difference data in IP surveys.

In SSIP, the acquired potential signal in one period can be modeled as

$$U = U_o + N, \tag{5}$$

where U_o denotes the standard potential signal and N denotes the added noise. The correlation between the acquired potential signal U and the transmitted (primary) current I is therefore given as

$$C_{(U,I)} = \frac{\sum_{i=1}^{n}(U_i - \bar{U})(I_i - \bar{I})}{\sqrt{\sum_{i=1}^{n}(U_i - \bar{U})^2 \sum_{i=1}^{n}(I_i - \bar{I})^2}}, \tag{6}$$

where $\bar{U}$ and $\bar{I}$ are the mean value of the noisy potential difference U and injected primary current I, respectively, and n denotes the number of potential or current samples in one period. Then, equation 5 was substituted to equation 6:

$$C_{(U,I)} = \frac{\sum_{i=1}^{n}(U_{0i} - \bar{U}_0)(I_i - \bar{I})}{\sqrt{\sum_{i=1}^{n}(U_i - \bar{U})^2 \sum_{i=1}^{n}(I_i - \bar{I})^2}} + \frac{\sum_{i=1}^{n}(N_i - \bar{N})(I_i - \bar{I})}{\sqrt{\sum_{i=1}^{n}(U_i - \bar{U})^2 \sum_{i=1}^{n}(I_i - \bar{I})^2}}, \quad (7)$$

where $\bar{U}_0$ and $\bar{N}$ are the mean value of standard potential signal U_0 and added noise N, respectively. Because the current signal I and noise N are generally not correlated (at least for noise coming from spurious sources that are located outside the survey system itself), this method is used to identify good data. Note that electromagnetic coupling and capacitive coupling between cables cannot be identified by this method. Increasing the distance between the transmitting cable and the receiving cable can reduce capacitive and EM couplings. The distance between the transmitting cable and receiving cable is kept at least at 50 m to reduce such couplings in our survey. It follows that the term

$$\sum_{1}^{n}(N_i - \bar{N})(I_i - \bar{I}) \approx 0, \quad (8)$$

and therefore,

$$C_{(U,I)} \approx \frac{\sum_{i=1}^{n}(U_{0i} - \bar{U}_0)(I_i - \bar{I})}{\sqrt{\sum_{i=1}^{n}(U_i - \bar{U})^2 \sum_{i=1}^{n}(I_i - \bar{I})^2}}. \quad (9)$$

$$C_{(U,I)} \approx \frac{\sum_{i=1}^{n}(U_{0i} - \bar{U}_0)(I_i - \bar{I})}{\sqrt{\sum_{i=1}^{n}(U_{0i} - \bar{U}_0 + N_i - \bar{N})^2 \sum_{i=1}^{n}(I_i - \bar{I})^2}}. \quad (10)$$

Because the measured potential signal U_o and injected current I are stationary, when the noise variance is high, the correlation coefficient of contaminated potential U and supplying current I is low.

Actual noise and simulated noise analysis

In our survey area, the recorded potential signals suffer from strong EM interferences possibly coming from at least three nonferrous metal smelters in operation at the mine site during the acquisition of the data. These smelters' use is indeed powered by high-power electric sources. In addition, a drilling machine was in operation near the data acquisition station. On the top of these spurious signals, the data were contaminated by the 50 Hz power line interference (and its harmonics), radio communication interferences, and other environmental noises located in the vicinity of the survey line. The 50 Hz power line interference is not a problem because the frequency band of SIP acquisition is only 1/16–1 Hz. The attenuation of digital decimation filter is greater than 120 dB. We found that the stray current caused by the mining and drilling processes was the major causes of EM interferences. The use of a low-pass RC filter applied before the preamplifiers is good enough to suppress the radio communication interferences because the frequency band associated with radio communications is much greater than the frequency band of the IP data.

Background noises were acquired before the current injection at different sites, and they can be mostly divided into two types (Figure 4). The first type of noise is a continuous noise caused by environmental interferences and can be seen as a stationary signal. For this noise, the mean stack approach is the most effective processing method because the average of such a random noise amplitude is nearly zero. The second major component of the noise is observed to be a discontinuous strong EM interference caused by cultural activity including production activity, drilling operations, and other electric power sources. For this second interference, the noise amplitude in different segments was changing significantly. Amplitude distribution of this noise is unsymmetrical, and its average is not equal to zero. This paper focuses on the recognition and elimination of these discontinuous interferences.

To analyze the influence of different noise amplitudes on the SSIP signal, high-quality measured potential difference data and associated primary current data are first used as the standard signals. The potential difference data set is contaminated with simulated noises with mean zero and various standard deviations. The standard potential, the current signal, and an example of potential data contaminated by the added synthetic noise are shown in Figure 5. Subsequently, the correlation coefficients between the contaminated potential and primary injected current, the S/N of the potential data, and the error of apparent resistivity are calculated and compared when the root-mean square (rms) of the noise ranges from 0.5 to 10 (rms is used to measure the power of the noise). The correlation coefficients were calculated using equation 6, the apparent resistivity data were calculated using equation 1, and the error was calculated using the following equation:

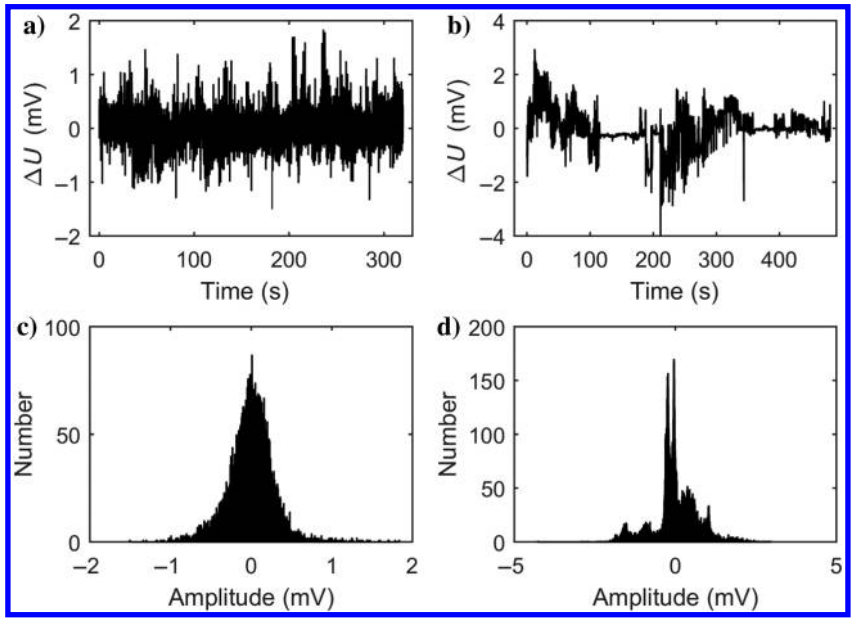

Figure 4. Two types of background noises acquired in the field prior the current injection. (a) Continuous noise caused by environmental interferences. (b) Discontinuous strong EM interferences caused by cultural activity. (c) Histogram of the continuous noise. (d) Histogram of the discontinuous noise.

Downloaded 08/31/18 to 93.174.129.117. Redistribution subject to SEG license or copyright; see Terms of Use at http://library.seg.org/

$$\varepsilon = 100\left|\frac{\rho_n - \rho_0}{\rho_0}\right|(\text{in}\%), \tag{11}$$

where ρ_0 denotes the apparent resistivity calculated using current data and potential data without simulated noise and ρ_n denotes the apparent resistivity calculated using current data and the potential data with the simulated noise added to them. The S/N of the contaminated potential signal was calculated according to

$$\text{S/N} = \log_{10}\left[\frac{\sum_{i=1}^{n}(U_{0i} - \bar{U}_0)^2}{\sum_{i=1}^{n}(N_i - \bar{N})^2}\right], \tag{12}$$

where U_0 is the standard potential signal and N denotes the simulated noise. Figure 6 shows the results for the correlation coefficients, S/N, and apparent resistivity errors. From Figure 6, we can see that the correlation coefficients and S/N decrease with increasing the noise power. When the rms of the noise is smaller than 4, the correlation coefficient is larger than 0.5, the S/N is larger than 0 dB, and the apparent resistivity error is less than 10%. This threshold can be used to meet approximately the requirement of data quality. In other words, a value of 0.5 for the correlation coefficient can be used as a threshold to decide the fate of the data. This is done for our survey as explained below.

We use now the data filtering method described above to detect and extract SSIP measurements with high S/N from the original data set contaminated by the simulated discontinuous noise. The multiperiod current data and the synchronous multiperiod potential data were used as the reference signals. Then, simulated discontinuous interferences are added to these reference potential data, and the correlation coefficients between the contaminated potential data and the primary current data of different segments were calculated.

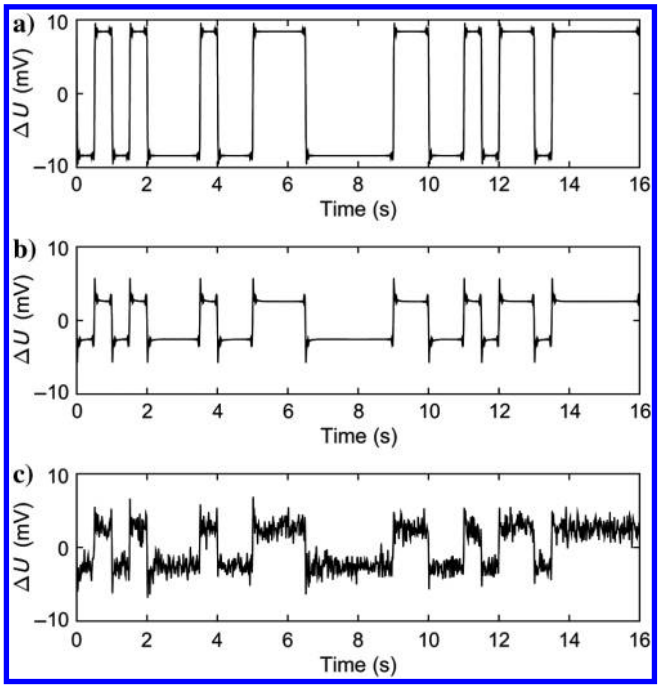

Figure 5. Obtention of the contaminated data. (a) Injected current sequence $I(t)$ (t is the time) at one period (16 s). (b) Measured reference potential signal $\Delta U(t)$ in the synchronous period. (c) The potential time series $\Delta U(t)$ is contaminated by some synthetic noise.

Finally, the high-quality data and the bad data were extracted, respectively, according to the threshold value of the correlation coefficient. Figure 7 shows the reference current data, the potential data, and the simulated discontinuous interferences. Figure 8 shows the contaminated potential data, the correlation coefficients, and the extracted potential data for different segments.

Correlation analysis of acquired actual contaminated potential signal

Then, we used the acquired actual contaminated potential signal and the associated primary current data to analyze the correlation coefficients and data quality for each period. Two test examples of data, acquired in the survey points no. 44 and no. 96 (i.e., when current electrodes A and B are located at −2200 and 2200 m) are used for the test. For the survey point no. 44, the potential electrodes M and N are located at −60 and −80 m. For the survey point no. 96, the potential electrodes M and N are located at 900 and 920 m. In these survey points, the potential difference and primary current data of 160 periods were acquired. In survey point no. 96, the potential response is high and EM interference is relatively weak. Figure 9 shows the injected primary current and the acquired potential signals in one synchronous period (16 s). Figure 9 shows that the potential data and current data are characterized by a high S/N. Then, we determine the correlation of the current data and potential data using equation 6, and we compute the apparent complex resistivity through equation 1 in each period, respectively. The apparent phase and apparent amplitude of the resistivity at four frequencies and the correlation coefficient for all the 160 periods are shown in Figure 10. In Figure 10a, the correlation coefficients

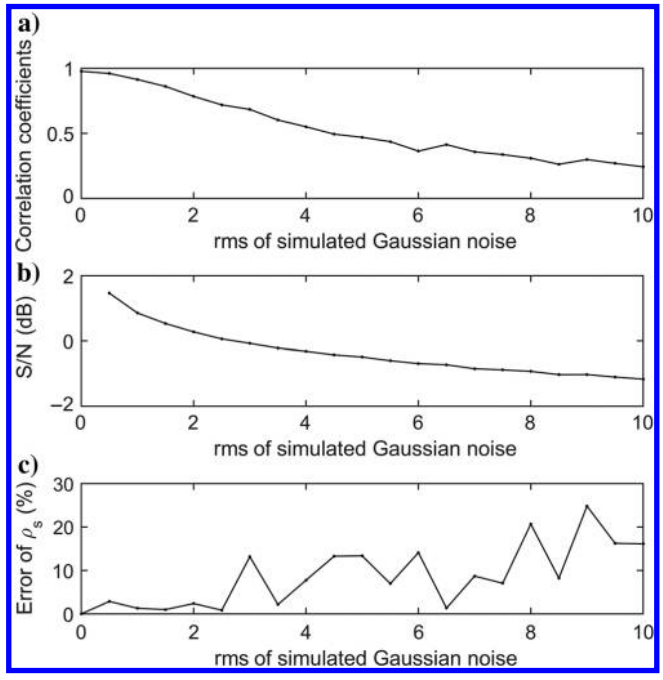

Figure 6. The effect of different levels (with rms range from 0 to 10) of Gaussian noise to the measured potential signals. (a) Correlation coefficients between the contaminated potentials and the supplying currents. (b) The S/N of the contaminated potential signal. (c) Apparent resistivity error when the rms-simulated Gaussian noise ranges from 0 to 10.

Downloaded 08/31/18 to 93.174.129.117. Redistribution subject to SEG license or copyright; see Terms of Use at http://library.seg.org/

Downloaded 08/31/18 to 93.174.129.117. Redistribution subject to SEG license or copyright; see Terms of Use at http://library.seg.org/

between the injected currents and the measured potentials are higher than 0.9 in most periods; meanwhile, the results of apparent phase (see Figure 10b) and resistivity (Figure 10c) appear stationary for most segments. However, in some segments including the 15–20 periods, 30–35 periods, and 50–55 periods (and few others), the correlation coefficient decreases slightly. There are also some slight deviations of apparent resistivity and phase in the corresponding segments shown in Figure 10b and 10c.

The potential response at survey point no. 44 is in contrast with the response shown previously. The S/N is low, and the noise interference appears to be much stronger. The cause of this difference may be associated with the presence of EM interferences associated with a drilling machine that was working in the vicinity of the survey point. We determine the correlation coefficients and apparent complex resistivity in each period for this survey point (see Figure 11). The correlation coefficients in most periods are less than 0.5 because of the strong EM interferences. Only the correlations in the first 20 periods are stable with values higher than 0.5 (Figure 11a). The apparent complex resistivity for these 20 periods is also stable. When the correlation coefficient decreases below 0.5, there is a great deviation in the apparent phase and apparent resistivity data (as we can see from Figure 11b and 11c). In this case, the phase deviation is more than 1000 mrad, and the resistivity deviation is more than 100 Ωm. In some periods, the correlation coefficients appears even to be negative. This phenomenon could be attributed to the vibration of the drilling machine near the potential electrodes M and N. Indeed, the vibration of the ground may change the contact resistance of these potential electrodes during the acquisition of the data. In turn, the change in the contact resistances can change the recorded potentials at the voltage electrodes, and the correlation between the acquired noisy voltages and the injected current may be slightly negative. These data segments were also discarded for further processing and tomography. Figure 12 shows the injected current and the measured potential signals when the correlation coefficient is 0.12 (below the threshold) and 0.65 (above the threshold), respectively. In Figure 12b, the original potential signals are distorted by the presence of the strong EM inter-

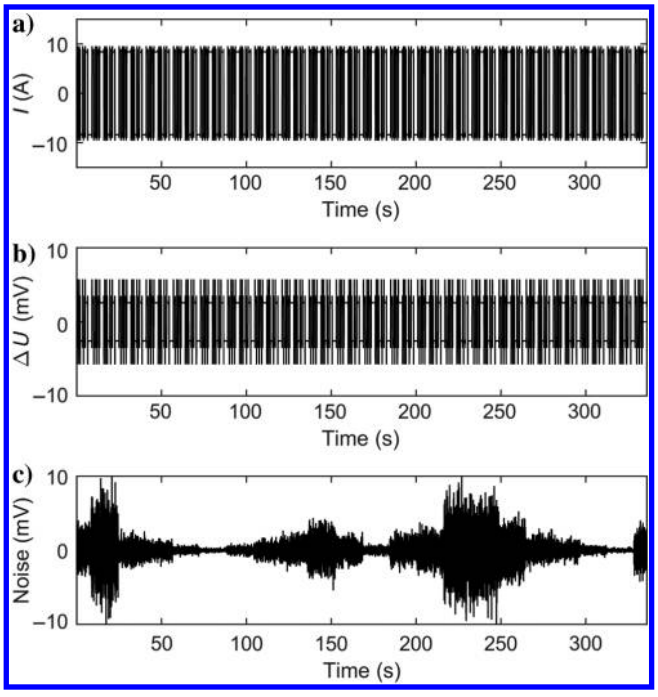

Figure 7. Time series of multiperiod current, potential, and simulated spike interferences. (a) The standard multiperiod current data. (b) Synchronous multiperiod potential data. (c) Simulated discontinuous interferences.

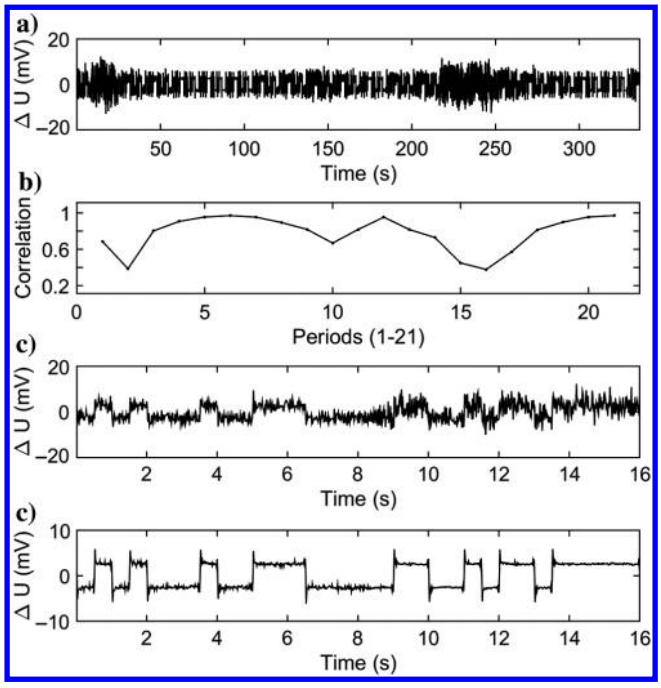

Figure 8. Potential signal contaminated by simulated spike interferences and corresponding correlation coefficients. (a) Potential signal contaminated by the simulated noise, (b) correlation coefficients between the contaminated potential and the supplying current in different segments, (c) the potential signal when the correlation coefficient is at 0.45, and (d) the potential signal when the correlation coefficient is 0.75.

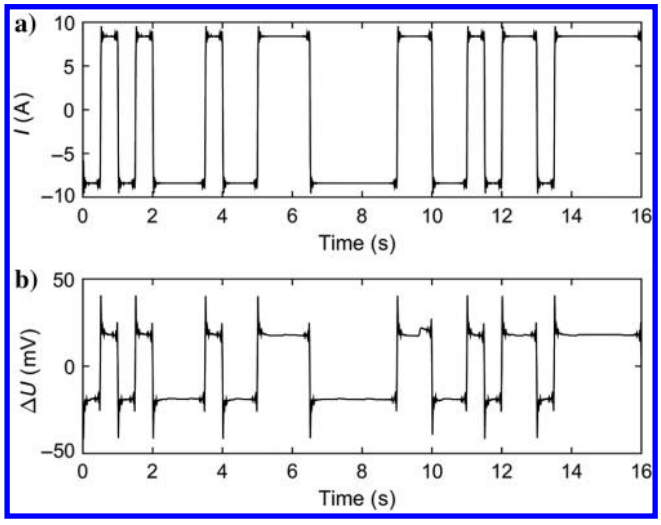

Figure 9. Time series of current $I(t)$ and measured potential signal $\Delta U(t)$ characterized a low noise level. (a) Supplying current $I(t)$ in one period for the survey point no. 96. (b) Acquired potential signal $\Delta U(t)$ in the synchronous period.

Downloaded 08/31/18 to 93.174.129.117. Redistribution subject to SEG license or copyright; see Terms of Use at http://library.seg.org/

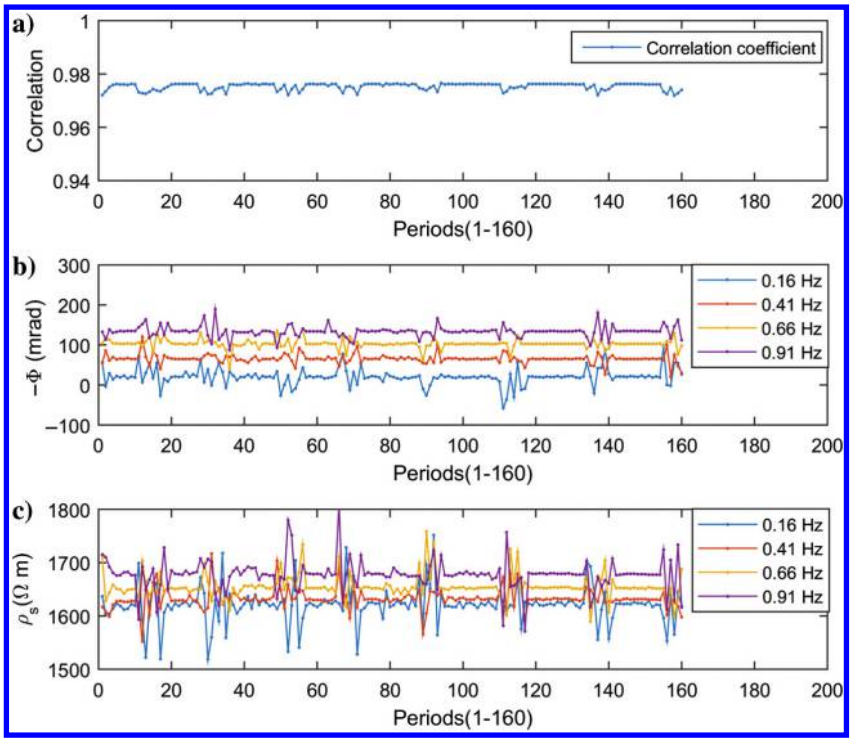

Figure 10. Correlation coefficients and complex resistivity computed from the high-quality signals. (a) Correlation coefficients of potential difference and supplying current for each period (160 periods in total) in survey point no. 96. (b) Apparent phase calculated using data in each period. (c) Apparent resistivity calculated using data in each period.

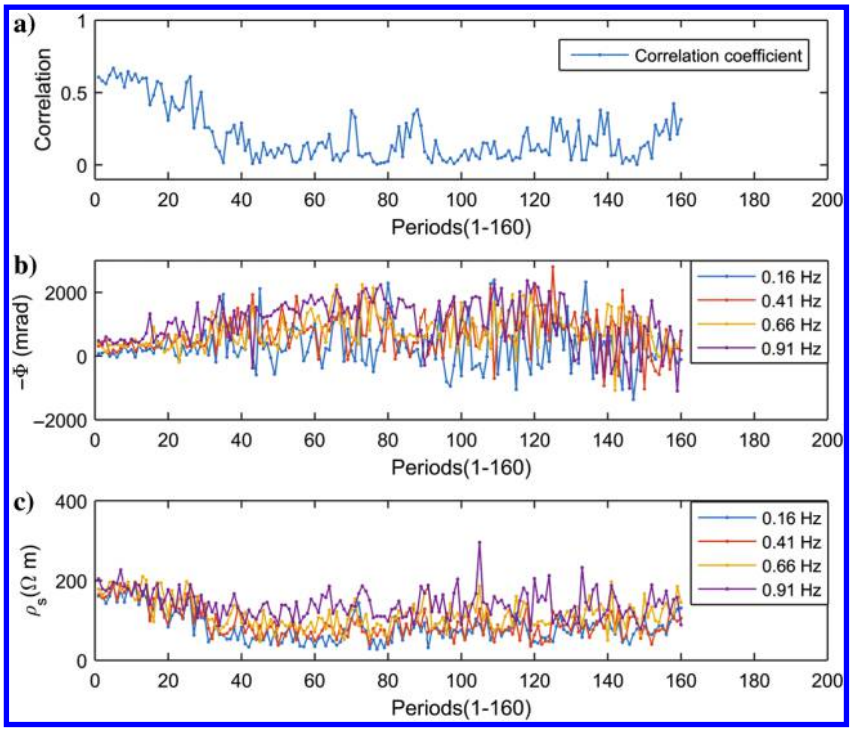

Figure 11. Correlation coefficients and complex resistivity computed from the low-quality signals. (a) Correlation coefficients of potential difference and supplying current for each period (160 periods in total) in survey point no. 44. (b) Apparent phase calculated using data in each period. (c) Apparent resistivity calculated using data in each period.

ferences, which should be rejected before stacking. In contrast, in Figure 12c, the potential data are contaminated by relative weak EM interferences, which can be used for stacking and subsequent processing.

We finish this section with a remark. For the SSIP data measured in the same survey point over a long time period, the correlation coefficients between the injected primary current and the measured potential in different segments are mostly affected by noise present in the measured potential signals. Indeed, there is almost no noise in the injected current, which can help us to select the good data and filter out the noisy data from original SSIP data before stacking. This procedure yields more accurate apparent complex resistivity results that can be further processed and used for tomography.

APPLICATION TO SSIP DATA PROCESSING

Calculation error of complex resistivity for survey points with different S/N

To demonstrate the effectiveness of the correlation analysis method, we use the original SSIP data with different S/Ns in two typical survey stations: stations no. 96 and no. 44. This is done to compute the apparent complex resistivity and compare their uncertainties. For each survey point, we adopt a mean stacking and correlation analysis method to process the SSIP data and to calculate the apparent complex resistivity data. For the first method, the current data and potential data in all the periods are stacked, and then, the apparent complex resistivity at four frequencies is determined using equation 1. For the second method, we compute the correlation coefficients for the current and potential data for each period. Then, we set a threshold to extract the high-quality data and remove the noisy data. When the mean value of the correlation coefficient for 160 periods is higher than 0.5, the value 0.5 is set as the threshold. When the mean value of the correlation coefficient for 160 periods is lower than 0.5 and the maximum correlation coefficient is higher than 0.5, the value 0.5 is set as the threshold. When the maximum correlation coefficients of all the periods is lower than 0.5, the quality of original data of all the periods is considered to be very poor, so new measurements at this survey point are required. After correlation analysis, only the data with high quality are used for stacking and to calculate the apparent complex resistivity data used for the tomography.

At survey points no. 96 and no. 44, the potential difference and the supplying current data of 160 periods have been acquired. First, the origi-

Downloaded 08/31/18 to 93.174.129.117. Redistribution subject to SEG license or copyright; see Terms of Use at http://library.seg.org/

nal potential and current data were divided into two groups. The first group corresponds to the 1–80 periods, and the second group corresponds to the 81–160 periods. Then, we used the method described above to process these two groups of data and to calculate the apparent complex resistivity data. The quantities ρ_1 and φ_1 denote the apparent resistivity and phase calculated using the 1–80 periods data, and ρ_2 and φ_2 are the results calculated using the 81–160 periods data. Then, we estimated the relative error of complex resistivity measurement to determine the data quality using

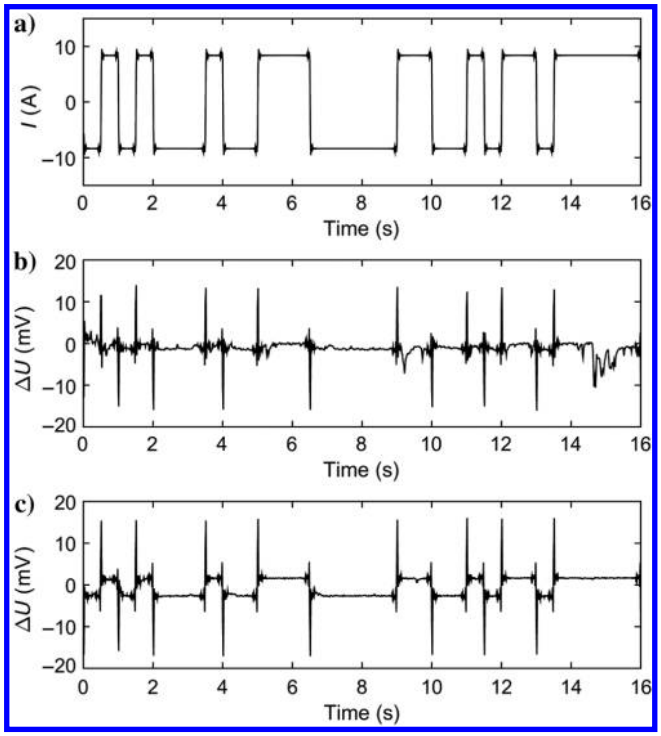

Figure 12. Time series of current signal and potential signal with low- and high-data quality. (a) Supplying current in one period for the survey point no. 44. (b) Acquired potential signal when the correlation coefficient is 0.12. (c) Acquired potential signal when the correlation coefficient is 0.65.

$$\varepsilon_\rho = 100\left|\frac{(\rho_1-\rho_2)/2}{(\rho_1+\rho_2)/2}\right|(\text{in}\%) \tag{13}$$

and

$$\varepsilon_\varphi = 100\left|\frac{(\varphi_1-\varphi_2)/2}{(\varphi_1+\varphi_2)/2}\right|(\text{in}\%), \tag{14}$$

where ε_ρ and ε_φ denote the errors associated with the apparent resistivity and phase, respectively. We took $(\rho_1+\rho_2)/2$ and $(\varphi_1+\varphi_2)/2$ as the final results.

The computations of the results and their associated error bars using and not using the correlation analysis for survey points no. 96 and no. 44 are provided in Tables 1 and 2. For the survey points characterized by a high S/N, such as no. 96 (Table 1), the calculated complex resistivity and error show a good consistency between the two approaches (i.e., with and without correlation analysis). However, for the survey stations characterized by low S/N, such as station no. 44 (see Table 2), the obtained results and associated uncertainties are quite different. Indeed, after using the correlation analysis, the apparent phase errors decrease from the range of 110–700 to 18–64 mrad. Meanwhile, the apparent resistivity error decreased from 28–43 to 6–16 Ωm, so the apparent complex resistivity data are clearly more accurate after using the correlation analysis.

Table 1. Apparent complex resistivity and error for survey point no. 96. The numbers 1 and 2 represent the results and errors using mean stack (averaging) method without correlation analysis and mean stack (averaging) with correlation analysis, respectively.

Frequency (Hz)	0.16	0.41	0.66	0.91
Phase 1 (mrad)	20.7 ± 3.8	65.9 ± 2.6	102.8 ± 2.6	133.5 ± 0.4
Phase 2 (mrad)	20.0 ± 0.5	65.1 ± 0.3	102.8 ± 0.4	134.4 ± 0.2
Resistivity 1 (Ωm)	971.8 ± 2.9	979.2 ± 0.8	992.8 ± 0.2	1005.7 ± 3.2
Resistivity 2 (Ωm)	972.9 ± 0.5	978.2 ± 0.6	991.2 ± 0.3	1007.0 ± 0.2

Table 2. Apparent complex resistivity and error for survey point no. 44. The numbers 1 and 2 represent the results and errors using mean stack (averaging) method without correlation analysis and mean stack (averaging) with correlation analysis, respectively.

Frequency (Hz)	0.16	0.41	0.66	0.91
Phase 1 (mrad)	339.3 ± 111.1	1016.6 ± 697.6	1028.6 ± 538.0	1157.3 ± 286.6
Phase 2 (mrad)	127.5 ± 56.9	298.6 ± 18.0	385.6 ± 64.3	487.2 ± 45.4
Resistivity 1 (Ωm)	44.8 ± 43.0	52.9 ± 43.1	74.8 ± 28.4	89.5 ± 34.9
Resistivity 2 (Ωm)	155.4 ± 5.5	161.5 ± 7.6	170.5 ± 13.0	180.1 ± 15.6

Downloaded 08/31/18 to 93.174.129.117. Redistribution subject to SEG license or copyright; see Terms of Use at http://library.seg.org/

Apparent complex resistivity and phase pseudosections

To further validate the apparent complex resistivity calculated using the correlation analysis method, we apply this processing to all the SSIP data for the survey line when the distance *AB* between the current electrodes range from 20 to 5200 m. Then, we calculate the apparent complex resistivity and relative phase at four frequencies for different values of AB. The pseudosections of apparent resistivity and apparent phase at four frequencies are shown in Figure 13 with and without using the correlation analysis. Figure 14 shows the pseudosections of the apparent phase for comparison using the same approach. For the full profiles, the horizontal distance ranges

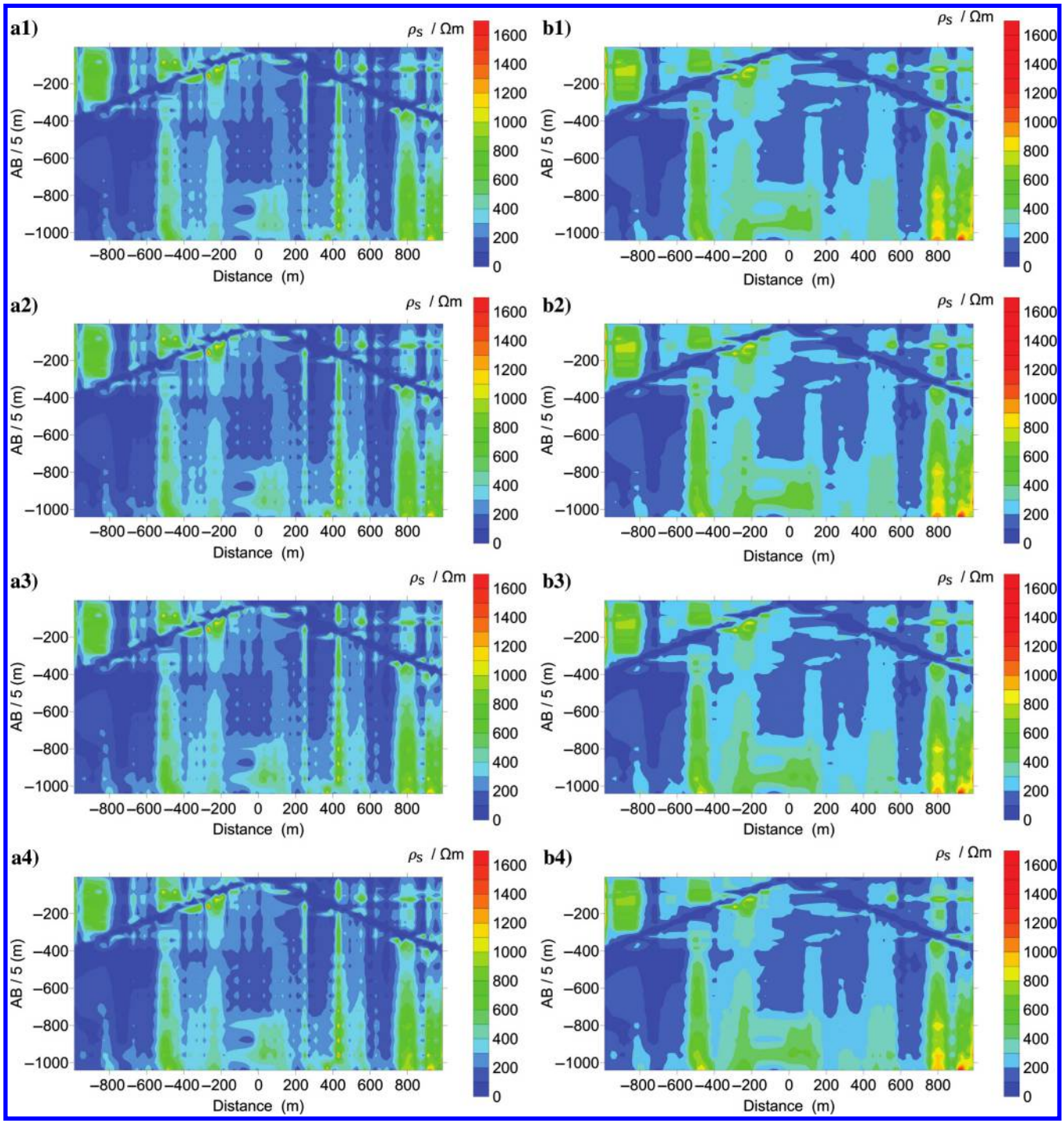

Figure 13. Pseudosections of apparent resistivity at (a1) 0.16 Hz, (a2) 0.41 Hz, (a3) 0.66 Hz, and (a4) 0.91 Hz without using correlation analysis. Pseudosections of apparent resistivity at (b1) 0.16 Hz, (b2) 0.41 Hz, (b3) 0.66 Hz, and (b4) 0.91 Hz using correlation analysis.

from −990 to 990 m, and the pseudodepths $AB/5$ range from 4 to 1040 m. The pseudosections at four frequencies can provide more information compared with measurements at single frequency especially for ore bodies (for the modeling of the spectral response of disseminated semiconductor in a porous material, see, for instance, Revil et al., 2015a, 2015b). We can see that there is a significant deviation in the apparent phase and apparent resistivity after using the correlation analysis. The resulting complex resistivity data obtained without using the correlation analysis for these stations are contaminated by noise interferences. In contrast, the resulting complex resistivity data using the correlation analysis appear more reasonable because the noisy data point has disappeared and the target anomaly seems enhanced. After denoising, there is indeed an anomaly of high-phase and low-resistivity amplitude located from the curvilinear position −200 to 200 m along the profile. This anomaly is further interpreted below by inverting the complex

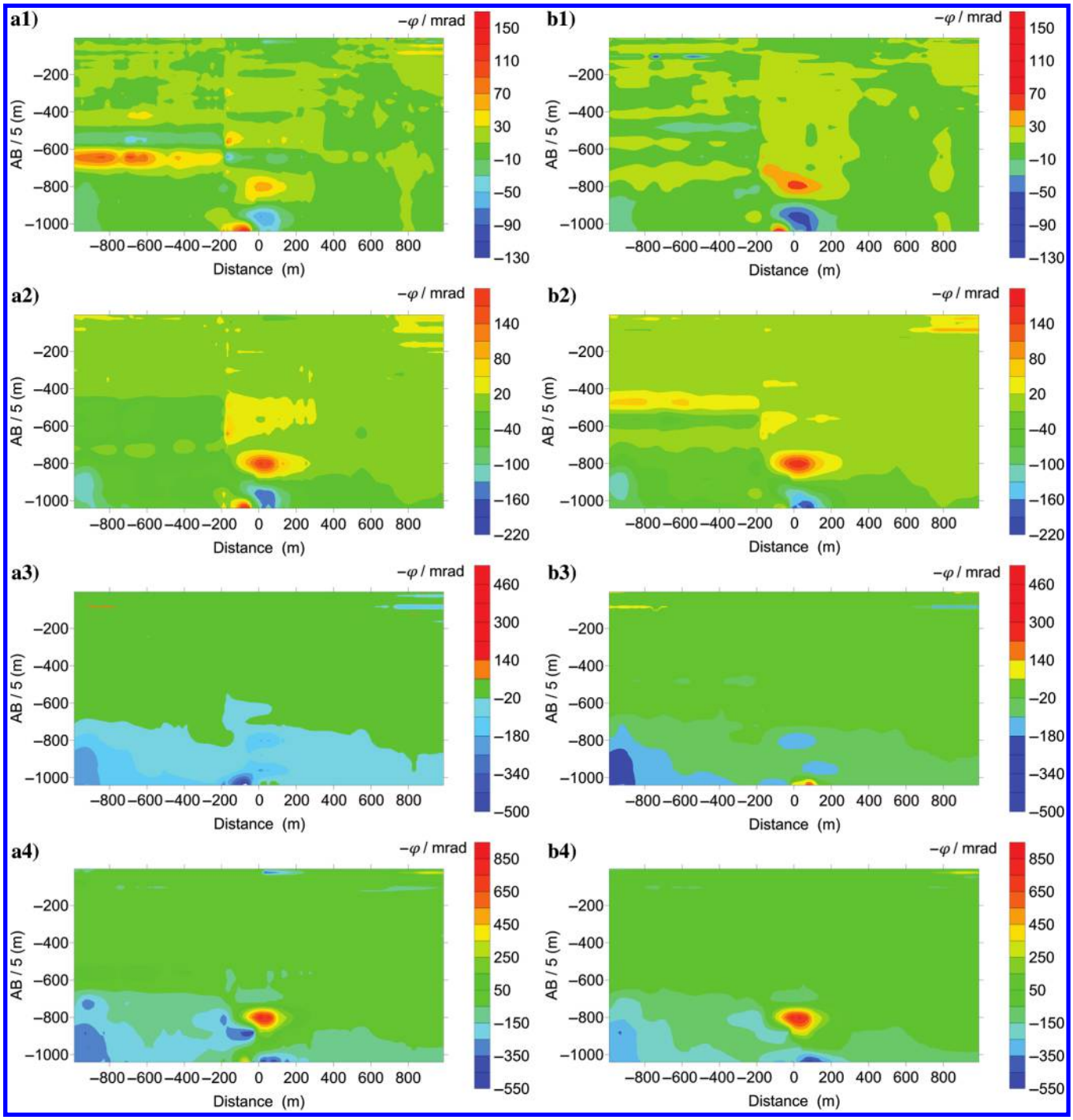

Figure 14. Pseudosections of apparent phase at (a1) 0.16 Hz, (a2) 0.41 Hz, (a3) 0.66 Hz, and (a4) 0.91 Hz without using correlation analysis. Pseudosections of apparent phase at (b1) 0.16 Hz, (b2) 0.41 Hz, (b3) 0.66 Hz, and (b4) 0.91 Hz using correlation analysis.

Downloaded 08/31/18 to 93.174.129.117. Redistribution subject to SEG license or copyright; see Terms of Use at http://library.seg.org/

Downloaded 08/31/18 to 93.174.129.117. Redistribution subject to SEG license or copyright; see Terms of Use at http://library.seg.org/

resistivity data and comparing the results with the existing geologic information.

In some pseudosections, when the current electrode space AB is large, the apparent phase values are positive. The presence of these positive phases can be associated with the distribution of array sensitivity and chargeable units (i.e., the pore bodies). These data should not be misled with the noise contaminated data and therefore should not be removed from the data set because they are associated with the targets (Dahlin and Loke, 2015). In the following, we use the positive and negative phase values in the tomography. In addition, to suppress the EM coupling in the original apparent complex resistivity data, the relative phase spectrum measurements were also used in the inversion procedure (Chen et al., 2009).

Inversion results and interpretation

We inverted the resistivity and IP data to check our approach. The data are inverted by ZondRes2D. The thickness of the first layer is set up to be 10 m, and the incremental factor for the next layers is 5%.The total number of layers is 42, and the maximal depth is 1352 m for the inversion. The fitting error is 9.9% for the resistivity data and 21.5% for the relative phase data. The big fitting error may be caused by the strong 3D topography for the near-surface part of the survey plus the strong EM couplings when the current electrode spacing is greater than 4000 m. Figure 14 shows clearly the effect of EM coupling at large current electrode spacings. Figure 15 shows the result of resistivity and chargeability and the location and shape of the known Pb-Zn ore body defined by eight wells.

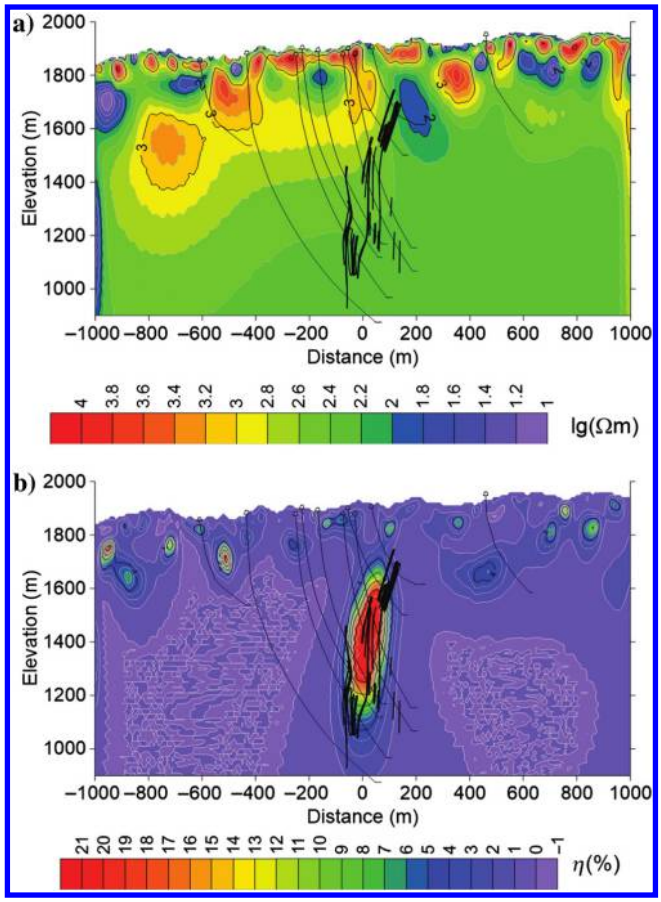

Figure 15. Final tomogram with topography. (a) The 2D resistivity model and (b) 2D IP model (chargeability). Both tomograms are derived from the apparent complex resistivity data at 0.41 Hz. The thick black lines show the shape and location of Pb-Zn ore bodies defined by the eight wells. The thin black lines show the location of 10 wells. The location of these wells is not exactly in the plan of the profile.

Figure 15a shows the resistivity model derived from the apparent resistivity data at 0.16 Hz. We found that the resistivity model correlates to the known fault and geologic structure very well. The location and shape of the Pb-Zn ore body are also shown in the figure. The ore-body is in a zone of transition from high resistivity to low resistivity. However, we cannot determine the exact location of the ore body from the resistivity data alone. This is quite consistent with the results obtained recently by Mao and Revil (2016) demonstrating that resistivity is not a good indicator of ore bodies.

Figure 15b shows the results in term of chargeability, which is known to be directly proportional to the volume content of metallic grains (Revil et al., 2015a, 2015b). The chargeability tomogram shows a clear highly chargeable anomaly associated with the position of the fault zone. Although the fitting error of the apparent phase data is 21.5% (a relatively high value), and the shape and location of the chargeable body are consistent with the position of the ore body (Figure 15b). We found that the fitting error is the largest in the area located directly below the ore body. This is likely due to strong EM coupling effects with the ore body itself. The resistivity and IP inversion including EM induction may produce a better result, and we plan to devote future works to investigate these effects.

CONCLUSION

We have developed a simple and effective correlation analysis approach to extract high-quality data from noisy IP data based on the SSIP approach. The essence of the correlation analysis is to extract data with high S/N and eliminate data with low S/N from the original SSIP data before stacking. Only data with high quality are retained for subsequent processing and tomography. This method is applied to a multiperiod SSIP 2D data set obtained in China and contaminated by strong EM interferences associated with mining operations and drilling activities. The correlation analysis method produces a better complex resistivity data set with a low level of errors compared with traditional methods. Because the principle of correlation analysis is very simple, the PMCC algorithm can be easily implemented on a laptop computer, which can allow the use of the SSIP data processing in the field, and the acquisition procedure can be improved in the field to improved data quality.

When original data in all the periods are contaminated by strong EM interference, correlation analysis processing is not enough to suppress noise. Under these circumstances, stronger injected primary currents and longer time acquisition times are necessary. In addition, when there are coherent noises in the current and potential data, this method is less effective. However, this requirement can easily be met because there is almost no strong noise in the current data.

With the SSIP method, the complex resistivity and phase can be calculated at four frequencies with a single current injection. Therefore, it offers the opportunity of mineral discrimination (through spectral analysis of the computed response) and EM coupling re-

Downloaded 08/31/18 to 93.174.129.117. Redistribution subject to SEG license or copyright; see Terms of Use at http://library.seg.org/

moval. We inverted the processed apparent resistivity and relative phase data. The 2D resistivity model is consistent with the known geologic structure and borehole data. The chargeability anomaly shows a strong correlation with the presence of a known ore body in terms of location and shape. The relative phase is not good enough to totally suppress EM coupling effects when the current electrode spacing is greater than 4000 m. Lower signal frequencies, different array types, or resistivity and IP inversion procedures including EM induction effects are required to improve the data processing and imaging.

ACKNOWLEDGMENTS

This paper is supported by the Fundamental Research Funds for the Central Universities of Central South University, China. SSIP data were measured in Gansu Province, China, and were kindly supplied by Champion Geophysical Technology Ltd., China. We are grateful for the help of W. Hong, Y. Hong-Chun, S. Rui-Jie, S. Hong-Hua, and Q. Jie-Ting.

REFERENCES

Bahorich, M., and S. Farmer, 1995, 3-D seismic discontinuity for faults and stratigraphic features: The correlation cube: The Leading Edge, **14**, 1053–1058, doi: 10.1190/1.1437077.

Barker, R. D., 1981, The offset system of electrical resistivity sounding and its use with a multicore cable: Geophysical Prospecting, **29**, 128–143, doi: 10.1111/j.1365-2478.1981.tb01015.x.

Brown, R. J., 1985, EM coupling in multi-frequency IP and a generalization of the Cole-Cole impedance model: Geophysical Prospecting, **33**, 282–302, doi: 10.1111/j.1365-2478.1985.tb00435.x.

Buselli, G., and M. Cameron, 1996, Robust statistical methods for reducing sferics noise contaminating transient electromagnetic measurements: Geophysics, **61**, 1633–1646, doi: 10.1190/1.1444082.

Chen, R. J., Z. X. He, L. F. He, and X. J. Liu, 2009, Principle of relative phase spectrum measurement in SIP: 79th Annual International Meeting, SEG, Expanded Abstracts, 869–873.

Chen, R. J., Z. X. He, J. T. Qiu, L. F. He, and Z. X. Cai, 2010, Distributed data acquisition unit based on GPS and ZigBee for electromagnetic exploration: Instrumentation and Measurement Technology Conference (I2MTC), IEEE, Expanded Abstracts, 981–985.

Chen, R. J., W. B. Luo, and J. S. He, 2007, High precision multi-frequency multi-function receiver for electrical exploration: 8th International Conference on Electronic Measurement and Instruments (ICEMI'07), IEEE, Expanded Abstracts, 599–602.

Collett, L. S., 1959, Laboratory investigation of overvoltage, *in* J. R. Wait, ed., Overvoltage research and geophysical applications, International series of monographs on earth sciences: Pergamon, New York, 50–70.

Dahlin, T., and M. H. Loke, 2015, Negative apparent chargeability in time-domain induced polarisation data: Journal of Applied Geophysics, **123**, 322–332, doi: 10.1016/j.jappgeo.2015.08.012.

Duncan, P. M., A. Hwang, R. N. Edwards, R. C. Bailey, and G. D. Garland, 1980, the development and applications of a wide band electromagnetic sounding system using a pseudo-noise source: Geophysics, **45**, 1276–1296, doi: 10.1190/1.1441124.

Gayen, A. K., 1951, The frequency distribution of the product-moment correlation coefficient in random samples of any size drawn from non-normal universes: Biometrika, **38**, 219–247, doi: 10.1093/biomet/38.1-2.219.

Golomb, S. W., 1994, Shift-register sequences and spread-spectrum communications: Third International Symposium on Spread Spectrum Techniques and Applications, IEEE, Expanded Abstracts, 14–15.

Han, S. L., S. G. Zhang, J. X. Liu, H. J. Hu, and W. S. Zhang, 2013, Integrated interpretation of dual frequency induced polarization measurement based on wavelet analysis and metal factor methods: Transactions of Nonferrous Metals Society of China, **23**, 1465–1471, doi: 10.1016/S1003-6326(13)62618-7.

He, J. S., 1993, Dual-frequency IP: Transactions of Nonferrous Metals Society of China-English edition, **3**, 1–10.

Ilyichev, P. V., and V. V. Bobrovsky, 2015, Application of pseudo noise signals in systems of active geoelectric exploration (Results of mathematical simulation and field experiments): Seismic Instruments, **51**, 53–64, doi: 10.3103/S0747923915010089.

Junge, A., 1996, Characterization of and correction for cultural noise: Surveys in Geophysics, **17**, 361–391, doi: 10.1007/BF01901639.

Kuhn, G. M., 1973, The phi coefficient as an index of ear differences in dichotic listening: Cortex, **9**, 450–457, doi: 10.1016/S0010-9452(73)80043-7.

Lamarque, G., 1999, Improvement of MT data processing using stationary and coherence tests: Geophysical Prospecting, **47**, 819–840, doi: 10.1046/j.1365-2478.1999.00162.x.

Larsen, J. J., 2016, Model-based subtraction of spikes from surface nuclear magnetic resonance data: Geophysics, **81**, no. 4, WB1–WB8, doi: 10.1190/geo2015-0442.1.

Larsen, J. J., and A. A. BehrooZmand, 2016, Processing of surface-nuclear magnetic resonance data from sites with high noise levels: Geophysics, **81**, no. 4, WB75–WB83, doi: 10.1190/geo2015-0441.1.

Li, M., W. B. Wei, W. B. Luo, and Q. D. Xu, 2013, Time-domain spectral induced polarization based on pseudo-random sequence: Pure and Applied Geophysics, **170**, 2257–2262, doi: 10.1007/s00024-012-0624-z.

Liu, W. Q., R. J. Chen, H. Z. Cai, and W. B. Luo, 2016, Robust statistical methods for impulse noise suppressing of spread spectrum induced polarization data, with application to a mine site, Gansu province, China: Journal of Applied Geophysics, **135**, 397–407, doi: 10.1016/j.jappgeo.2016.04.020.

Liu, W. Q., R. J. Chen, H. Wu, J. T. Qiu, H. C. Yao, R. J. Shen, and P. Zeng, 2015, High precision FDIP exploration in productive mine with strong EM interference: Symposium on the Application of Geophysics to Engineering and Environmental Problems(SAGEEP 2015), EEGS, Expanded Abstracts, 65–73.

Mao, D., and A. Revil, 2016, Induced polarization response of porous media with metallic particles — Part 3. A new approach to time-domain induced polarization tomography: Geophysics, **81**, no. 4, D345–D357, doi: 10.1190/geo2015-0283.1.

Olsson, P. I., G. Fiandaca, and J. J. Larsen, 2016, Doubling the spectrum of time-domain induced polarization by harmonic de-noising, drift correction, spike removal, tapered gating and data uncertainty estimation: Geophysical Journal International, **207**, 774–784, doi: 10.1093/gji/ggw260.

Oppenheim, A. V., 1989, Discrete-time signal processing: Pearson Education India.

Pellerin, L., 2002, Applications of electrical and electromagnetic methods for environmental and geotechnical investigations: Surveys in Geophysics, **23**, 101–132, doi: 10.1023/A:1015044200567.

Pelton, W. H., S. H. Ward, P. G. Hallof, W. R. Sill, and P. H. Nelson, 1978, Mineral discrimination and removal of inductive coupling with multi-frequency IP: Geophysics, **43**, 588–609, doi: 10.1190/1.1440839.

Ramsey, P. H., 1989, Critical values for Spearman's rank order correlation: Journal of Educational and Behavioral Statistics, **14**, 245–253, doi: 10.3102/10769986014003245.

Reddy, I. K., and D. Rankin, 1974, Coherence functions for magnetotelluric analysis: Geophysics, **39**, 312–320, doi: 10.1190/1.1440430.

Revil, A., G. Z. Abdel Aal, E. A. Atekwana, D. Mao, and N. Florsch, 2015a, Induced polarization response of porous media with metallic particles — Part 2. Comparison with a broad database of experimental data: Geophysics, **80**, no. 5, D539–D552, doi: 10.1190/geo2014-0578.1.

Revil, A., N. Florsch, and D. Mao, 2015b, Induced polarization response of porous media with metallic particles — Part 1: A theory for disseminated semiconductors: Geophysics, **80**, no. 5, D525–D538, doi: 10.1190/geo2014-0577.1.

Routh, P. S., and D. W. Oldenburg, 2001, Electromagnetic coupling in frequency-domain induced polarization data: A method for removal: Geophysical Journal International, **145**, 59–76, doi: 10.1111/j.1365-246X.2001.00384.x.

Saraev, A. K., A. B. Nikiforov, N. E. Romanova, and I. S. Eremin, 2012, Possibilities of electric field measurements in the audio frequency range using ungrounded electric sensors: Seismic Instruments, **48**, 209–213, doi: 10.3103/S0747923912030115.

Schlumberger, C., 1920, Study of underground electrical prospecting: Paris, 99.

Seigel, H. O., 1959, Mathematical formulation and type curves for induced polarization: Geophysics, **24**, 547–565, doi: 10.1190/1.1438625.

Stigler, S. M., 1989, Francis Galton's account of the invention of correlation: Statistical Science, **4**, 73–79, doi: 10.1214/ss/1177012580.

Streich, R., M. Becken, and O. Ritter, 2013, Robust processing of noisy land-based controlled-source electromagnetic data: Geophysics, **78**, no. 5, E237–E247, doi: 10.1190/geo2013-0026.1.

Szarka, L., 1988, Geophysical aspects of man-made electromagnetic noise in the earth — A review: Surveys in Geophysics, **9**, 287–318, doi: 10.1007/BF01901627.

Tate, R. F., 1954, Correlation between a discrete and a continuous variable: Point-biserial correlation: The Annals of Mathematical Statistics, **25**, 603–607, doi: 10.1214/aoms/1177728730.

Wait, J. R., 1959, The variable-frequency method, *in* J. R. Wait, ed., Overvoltage research and geophysical applications: Pergamon, International series of monographs on earth sciences, 29–49.

Xi, X. L., H. C. Yang, L. F. He, and R. J. Chen, 2013, Chromite mapping using induced polarization method based on spread spectrum technology: Symposium on the Application of Geophysics to Engineering and Environmental Problems (SAGEEP 2013), EEGS, Expanded Abstracts, 13–19.

Xi, X. L., H. C. Yang, X. F. Zhao, H. C. Yao, J. T. Qiu, R. J. Shen, and R. J. Chen, 2014, Large-scale distributed 2D/3D FDIP system based on ZigBee network and GPS: Symposium on the Application of Geophysics to Engineering and Environmental Problems (SAGEEP 2014), EEGS, Expanded Abstracts, 130–139.

Ziolkowski, A., B. A. Hobbs, and D. Wright, 2007, Multitransient electromagnetic demonstration survey in France: Geophysics, **72**, no. 4, F197–F209, doi: 10.1190/1.2735802.

Zonge, K. L., and J. C. Wynn, 1975, Recent advances and applications in complex resistivity measurements: Geophysics, **40**, 851–864, doi: 10.1190/1.1440572.

Downloaded 08/31/18 to 93.174.129.117. Redistribution subject to SEG license or copyright; see Terms of Use at http://library.seg.org/

This article has been cited by:

1. Weiqiang Liu, Pinrong Lin, Qingtian Lü, Rujun Chen, Hongzhu Cai, Jianhua Li. 2017. Time Domain and Frequency Domain Induced Polarization Modeling for Three-dimensional Anisotropic Medium. *Journal of Environmental and Engineering Geophysics* **22**:4, 435-439. [Abstract] [Full Text] [PDF] [PDF w/Links]

Downloaded 08/31/18 to 93.174.129.117. Redistribution subject to SEG license or copyright; see Terms of Use at http://library.seg.org/